2024 IEEE/RSJ International Conference on Intelligent Robots and Systems (IROS)
October 14-18, 2024. Abu Dhabi, UAE

ICR-based Kinematics for Wheeled Skid-Steer Vehicles on Firm Slopes*

Jorge L. Martínez[1] (*Senior Member, IEEE*), Jesús Morales[1], Manuel Sánchez[1]
and Alfonso García-Cerezo[1] (*Senior Member, IEEE*)

Abstract— **This paper proposes a new kinematic model for wheeled skid-steer vehicles moving with low inertia on firm slopes that is based on the variation of the Instantaneous Center of Rotation (ICR) of its lateral treads. To this end, the ICR-based model for horizontal surfaces, where constant tread ICRs were considered, has been extended with two additional parameters to account for the sliding down phenomenon on inclined terrains that the former is unable to predict. The current pitch and roll angles of the vehicle together with the speeds of the treads are employed to calculate the changing positions of tread ICRs during turnings. This kinematic approach shows promising results when applied to the heavy robotic rover J8 on a slanted surface of smooth concrete.**

I. INTRODUCTION

Skid-steering is a locomotion system characterized by independently driving the parallel treads of a ground vehicle. Turning requires commanding different rotation speeds to each tread, which provokes that the outer tread in the turn is braked by the inner tread, which, conversely, is dragged by the outer. Thus, the outer tread slips, i.e., it advances less than the displacement given by its rotational speed, and the inner one skids, i.e., it progresses more than expected by its rotational speed. When the vehicle is turning on spot, ideally with opposite tread speeds, slipping happens on both treads. Only when both treads have the same rotational speed no slipping or skidding occurs (during straight line motion).

The treads of a skid-steer vehicle can be built with tracks or with several mechanically-linked wheels. The main difference is their contact patches with the ground, that is much bigger with tracks than with wheels, resulting in a higher friction and a better traction on irregular terrains [1]. The number of wheels per side usually varies between two and four, being the behavior of a tread with more wheels closer to a track.

Due to its mechanical simplicity and high maneuverability, skid-steering locomotion has been commonly adopted by both manned [2] and unmanned [3] ground vehicles. Field applications of skid-steer mobile robots include inspection [4], mining [5], agriculture [6][7], search and rescue [8] and forestry [9], among others.

Nevertheless, this mechanism implies high power requirements [10][11] and makes dynamic modeling more intricate [12][13]. Furthermore, operating on sloped terrain [14][15], especially on loose soil [16][17], or at high inertia [18][19] can cause uneven loading of the tractive surfaces.

Kinematics for skid-steered vehicles can be useful for improving motion control [20] and odometry [21] during autonomous navigation without the need of incorporating dynamics. The most popular model is based on the Instantaneous Center of Rotation (ICR) of the treads, which approximates the kinematics of both tracked [22] and wheeled [23] skid-steer mobile robots on horizontal hard-soil surfaces under low inertia.

ICR-based kinematics constitutes an extension of the differential-drive model by considering two virtual wheels situated at the tread ICRs. It has been successfully applied to different skid-steer vehicles mainly small-scale [24], but also medium-sized [25] and heavy ones [26]. It has also been employed for simulating their motion on synthetic environments [27][28].

The ICR-based model is able to implicitly take into account some dynamical effects and it can be customized to operate on different terrain types [29][30]. The local coordinates of tread ICRs for leveled terrains can be obtained through offline [22][23][31] and with online [19][32][33] experiments.

ICR-based kinematics can be simplified on vehicles with a symmetrical mass distribution by only using the distance between tread ICRs [34][35] or augmented to predict slippage using wheel accelerations [36], to model energy consumption [37][38][39] and to develop dynamics [40].

The behavior of tread ICRs on firm inclines has been analyzed in detail recently [41] and it cannot be captured properly by the ICR-based model, which is not prepared to operate with varying pitch and roll angles. As a continuation of this work, the paper proposes kinematics for wheeled skid-steer vehicles on firm slopes. The new model extends horizontal ICR kinematics with two extra parameters to take into account sliding down during turning. This kinematic model has been successfully identified and tested on the heavy robotic rover J8 moving on a concrete slope.

The rest of the paper is organized as follows. Next section reviews the previous works from which this proposal is based. Then, Section III presents the new ICR-based kinematic model on firm inclines, including parameter identification. The application to the robotic rover J8 is described in Section IV. The conclusions of this work can be found in Section V. Finally, the references complete the paper.

---

*This work was partially supported by the Spanish project PID2021-122944OB-I00.

[1] Institute for Mechatronics Engineering & Cyber-Physical Systems, Universidad de Málaga, 29071-Málaga, Spain `{jorgelmartinez, jesus.morales, manuel.sanchez.m, ajgarcia}@uma.es`

II. ICR-BASED KINEMATIC MODEL

The notation employed for ICR-based kinematics to describe skid-steered locomotion on hard soil is introduced below. Then, the main results on horizontal and inclined terrains are summarized.

Let the origin of the local reference frame XYZ of the vehicle be at the center of the rectangle defined by the wheel contact points with a flat surface, where Y is aligned with the forward motion direction, the Z axis points upwards and X to the right. Let also x_m and y_m be the minimum distances from the origin to the base rectangle along the X and Y axes, respectively.

Let α and ϕ be the roll and pitch angles of the axes X and Y in relation to a horizontal plane, respectively. Let γ be the angle of the Y axis of the vehicle with respect to the direction of the maximum slope β on the local XY plane (see Fig. 1). The following relations between these angles are fulfilled:

$$\alpha = -\beta \sin(\gamma), \quad \phi = \beta \cos(\gamma), \tag{1}$$

$$\tan(\gamma) = -\alpha/\phi, \tag{2}$$

$$\beta = \sqrt{\alpha^2 + \phi^2}. \tag{3}$$

Let v_x, v_y and ω_z be the lateral, longitudinal and angular velocities of the vehicle, respectively. Let V_l and V_r be the longitudinal speeds applied to every wheel of the left and the right treads, respectively. Kinematics tries to describe skid-steer locomotion by obtaining v_x, v_y and ω_z from α, ϕ, V_l and V_r, neglecting motor torques and vehicle accelerations (both, linear and angular).

The ICR of a vehicle is defined as the point on the XY plane where its motion can instantly be represented as a pure rotation. The ICR of each tread is different from the vehicle's ICR because its own rotation speed should also be considered.

Let (x^l_{ICR}, y_{ICR}) and (x^r_{ICR}, y_{ICR}) be the local coordinates of the ICRs for the left and the right treads, respectively, where both ICRs share the same Y coordinate [22]. Then, vehicle velocities on the local XY plane can be estimated as a function of lateral speeds with the following asymmetric model [23]:

$$\begin{pmatrix} v_x \\ v_y \\ \omega_z \end{pmatrix} = \frac{1}{x^r_{ICR} - x^l_{ICR}} \begin{pmatrix} -y_{ICR} & y_{ICR} \\ x^r_{ICR} & -x^l_{ICR} \\ -1 & 1 \end{pmatrix} \begin{pmatrix} V_l \\ V_r \end{pmatrix}. \tag{4}$$

A. Horizontal Surface Case

On hard horizontal terrain and under low inertia, tread ICRs of skid-steer vehicles remain almost with constant local coordinates outside of the tread contact lines, contrary to the vehicle's ICR that can be located at any point of the line that crosses tread ICRs [22]. The mean values for left and right tread ICRs on a given terrain type: $(\bar{x}^l_{ICR}, \bar{y}_{ICR})$ and $(\bar{x}^r_{ICR}, \bar{y}_{ICR})$, can be considered as the wheel contact points of an equivalent differential-drive vehicle [23].

In this way, ICR-based Horizontal Kinematics (ICRHK) requires three parameters: $\bar{x}^l_{ICR}$, $\bar{x}^r_{ICR}$ and $\bar{y}_{ICR}$. A symmetrical mass distribution around the Y axis of the vehicle avoids traction predominance of the left or right treads [22] and kinematics can be simplified using $\bar{x}^l_{ICR} = -\bar{x}^r_{ICR}$. Similarly, with a symmetrical mass distribution around the X axis, a balanced traction from front and rear wheels occurs and $\bar{y}_{ICR} = 0$ can be employed.

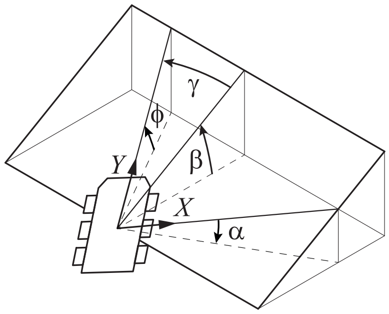

Fig. 1. Diagram of the angles α, β, γ and ϕ on the local XY plane of the vehicle.

B. Analysis on Inclined Terrain

The local coordinates of tread ICRs suffer relevant and continuous changes around the horizontal values when turning on hard-soil inclines with constant rotation speeds of the treads [41]. Nevertheless, both ICRs keep away from tread centerlines, but inside the contact lines with the ground of the front and rear wheels.

According to [41], changes on tread ICRs mainly depend on the current values of α, ϕ and $\text{sign}(V_r - V_l)$. The sign of $(V_r - V_l)$ has the effect of changing the displacement direction of both ICRs. On the other hand, $|V_r - V_l|$ seemed to have little influence. Neither was $|V_r + V_l|$ considered significant, but the maximum absolute value of longitudinal speed was limited to $v^m_y = 0.28\,\text{m}\,\text{s}^{-1}$ in the case study.

Alterations on tread ICRs have relevant effects on the traction of the vehicle. Thus, longitudinal shifts on tread ICRs, with y_{ICR} above or below 0, imply an emphasis in the traction of the front or rear wheels, respectively. On the other hand, lateral displacements of tread ICRs, with x^l_{ICR} and x^r_{ICR} moving both at the same time to the left or to the right, produce a predominance on the traction of the right or left treads, respectively, hindering turning [41].

Concretely, the traction of the outer tread in a turn tends to improve or to worsen when the vehicle is heading downwards or upwards, respectively, causing the vehicle to slide down, even on small inclines [41]. This situation aggravates when the vehicle is mainly pointing to the top (i.e., $-45^\circ < \gamma < 45^\circ$) or to the bottom (i.e., $135^\circ < \gamma < 225^\circ$).

III. ICR-BASED KINEMATICS ON SLOPES

Building on the results summarized in the previous section, ICR-based Inclined Kinematics (ICRIK) for wheeled skid-steered vehicles on slopes is proposed next.

Assuming smooth variations on β, V_l and V_r, this model extends ICRHK with two positive parameters (namely, λ_1 and λ_2) to estimate the changing coordinates of tread ICRs along a trajectory:

I: Calculation of x^l_{ICR}:

$$x^l_{ICR} = \bar{x}^l_{ICR} + \mathrm{sign}(V_r - V_l)\left(v^m_y - \frac{|V_r + V_l|}{2}\right)\lambda_1\,\phi. \tag{5}$$

II: Calculation of x^r_{ICR}:

$$x^r_{ICR} = \bar{x}^r_{ICR} + \mathrm{sign}(V_r - V_l)\left(v^m_y - \frac{|V_r + V_l|}{2}\right)\lambda_1\,\phi. \tag{6}$$

III: Calculation of y_{ICR}:

$$y_{ICR} = \bar{y}_{ICR} + \mathrm{sign}(V_r - V_l)\left(v^m_y - \frac{|V_r + V_l|}{2}\right)\lambda_1\,\alpha, \tag{7}$$

where:

$$\mathrm{sign}(V_r - V_l) = \begin{cases} 1, & \text{if } V_r > V_l, \\ -1, & \text{if } V_r < V_l, \\ 0, & \text{if } V_r = V_l. \end{cases} \tag{8}$$

Additionally, in the cases of aggravated sliding down:

I: If $(V_r > V_l \wedge -\phi > |\alpha|) \vee (V_r < V_l \wedge \phi > |\alpha|)$ then

$$x^l_{ICR} {+}= (1 - \left|\frac{\alpha}{\phi}\right|)\,\mathrm{sign}(V_r - V_l)\left(v^m_y - \frac{|V_r + V_l|}{2}\right)\lambda_2\,\phi. \tag{9}$$

II: If $(V_r > V_l \wedge \phi > |\alpha|) \vee (V_r < V_l \wedge -\phi > |\alpha|)$ then

$$x^r_{ICR} {+}= (1 - \left|\frac{\alpha}{\phi}\right|)\,\mathrm{sign}(V_r - V_l)\left(v^m_y - \frac{|V_r + V_l|}{2}\right)\lambda_2\,\phi. \tag{10}$$

Finally, the following limits should be taken into account:

I: If $x^l_{ICR} > -x_m$ then $x^l_{ICR} = -x_m$.
II: If $x^r_{ICR} < x_m$ then $x^r_{ICR} = x_m$.
III: If $|y_{ICR}| > y_m$ then $y_{ICR} = \mathrm{sign}(y_{ICR})y_m$.

ICRIK continually calculates the local coordinates of tread ICRs in order to apply (4). Firstly, (5)-(8) are obtained. Then, (9) or (10) are evaluated when their opposite triggering conditions are met. Lastly, the limitations are applied, if necessary.

Coordinates, x^l_{ICR} and x^r_{ICR} vary with the pitch angle, whereas y_{ICR} depends on the roll angle. When moving on horizontal terrain (i.e, with $\beta = 0°$) or in a straight line (i.e., with $V_l = V_r$), ICRHK is maintained.

The parameter λ_1 of ICRIK serves to expand tread ICRs according to the current roll and pitch angles in a circular way around the horizontal ICRs. On the other hand, λ_2 is employed to consider the extra traction loss of a tread in the aggravated sliding down cases (9) and (10), where the relation $0 < |\alpha/\phi| < 1$ applies, according to (1). The longitudinal speed of the vehicle (approximated by $|V_r + V_l|/2$) tends to mitigate the effect of both parameters, reducing deviations from ICRHK.

A. Application to the Mobile Robot Lazaro.

To further clarify (5)-(10), ICRIK has been applied to the case study presented in [41] with the four-wheeled mobile robot Lazaro, where $x_m = y_m = 0.2\,\mathrm{m}$. Experimental data was recorded when Lazaro was commanded with $V_l = -V_r = 0.21\,\mathrm{m/s}$ to turn clockwise on a melamine board tilted with different angles.

Fig. 2 shows both the experimentally estimated and model-based tread ICRs. The parameters for ICRHK were calculated as the mean values of the 0° tilting case as $\bar{x}^l_{ICR} = -0.44\,\mathrm{m}$, $\bar{x}^r_{ICR} = 0.42\,\mathrm{m}$ and $\bar{y}_{ICR} = 0.03\,\mathrm{m}$. The additional parameters for ICRIK were optimally adjusted on the remaining tilting cases as $\lambda_1 = 4.68\,\mathrm{s\,rad^{-1}}$ and $\lambda_2 = 6.54\,\mathrm{s\,rad^{-1}}$.

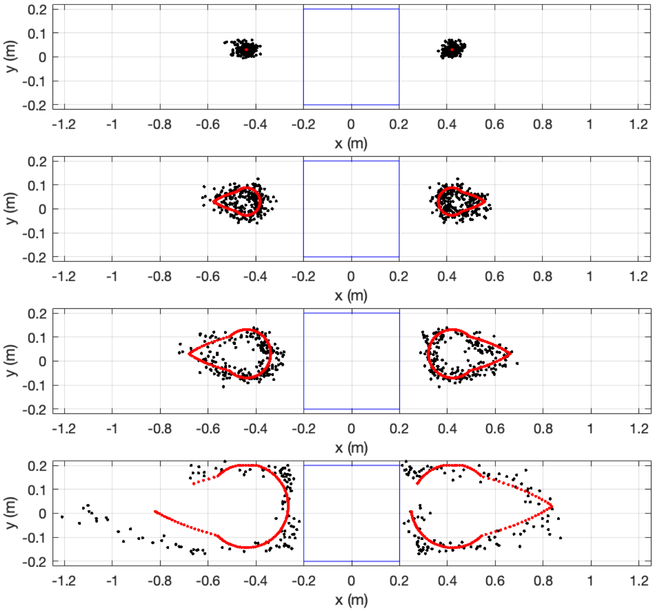

Fig. 2. Experimentally estimated and model-based tread ICRs plotted with black and red dots, respectively, on the local XY plane for tilting angles of the board of $0°, 2.5°, 4.4°$ and $7.6°$ from top to bottom. The base rectangle of Lazaro is represented with blue lines.

It can be observed in Fig. 2 that the coordinates of tread ICRs expands from the horizontal values with the tilting angle, which is modeled by the λ_1 parameter of ICRIK. The aggravated sliding down case on a tilted surface, which is captured by the λ_2 parameter, can be seen as the lobe of the ovals.

The distance between tread ICRs remains relatively constant with the exception of the aggravated sliding down cases where it grows. It is also visible in Fig. 2 that the limitation of y_{ICR} to y_m has been applied to the 7.6° tilting case.

B. Experimental Identification

First of all, it is necessary to introduce correction factors c_l and c_r to consider tire inflation conditions and mechanical misalignments [22][23] for adjusting measured speeds v_l and v_r to current tread speeds:

$$V_l = c_l\,v_l, \quad V_r = c_r\,v_r, \tag{11}$$

so when $V_l = V_r$, the vehicle does not deviate from straight line motion and the travelled distance coincides with the expected value.

The procedure to estimate the parameters of the new ICR-based model comprises two consecutive stages. The first stage involves experiments on a leveled flat surface by driving the vehicle manually on a given soil type with different velocities and radii of curvature to obtain the parameters of ICRHK together with c_l and c_r as in [23].

For the second stage, it is proposed to perform a single experiment on an inclined plane that consists on trying to turn on spot (i.e., $V_l = -V_r$) while the vehicle slides down to obtain the two additional parameters of ICRIK.

Data from both exteroceptive and proprioceptive sensors have to be recorded synchronously. Exteroceptive sensors, such as GNSS receivers, cameras or LiDARs, are needed to obtain a ground-truth trajectory of the vehicle composed of 2D and 3D poses for the first and second stages, respectively. On the other side, tread speeds together with pitch and roll angles from internal readings are employed by the kinematic model to replay the trajectory.

With the vehicle speed estimations (4), the following dead-reckoning equations can be applied:

$$\begin{pmatrix} x' \\ y' \\ z' \\ \psi' \end{pmatrix} = \begin{pmatrix} \mathrm{C}_\psi \mathrm{C}_\alpha & \mathrm{C}_\psi \mathrm{S}_\phi \mathrm{S}_\alpha - \mathrm{C}_\phi \mathrm{S}_\psi & 0 \\ \mathrm{S}_\psi \mathrm{C}_\alpha & \mathrm{C}_\psi \mathrm{C}_\phi + \mathrm{S}_\phi \mathrm{S}_\psi \mathrm{S}_\alpha & 0 \\ -\mathrm{S}_\alpha & \mathrm{S}_\phi \mathrm{C}_\alpha & 0 \\ 0 & 0 & \frac{\mathrm{C}_\phi}{\mathrm{C}_\alpha} \end{pmatrix} \begin{pmatrix} v_x \\ v_y \\ \omega_z \end{pmatrix}, \tag{12}$$

where ψ is the yaw angle of the vehicle with respect to a global reference frame with its X_g and Y_g axes on a horizontal plane and Z_g pointing upwards, and the letters C and S denote the cosine and sine functions, respectively.

By integrating (12) along time using measurements of α and ϕ, the 2D or 3D pose of the vehicle during the experiments can be deduced. Offline optimization is required to find the best parameters for each model, i.e., those that reduce dead-reckoning errors in position and heading.

The fitness J of a given set of parameters for a kinematic model can be calculated as the sum of the squared errors:

$$J = \sum \left(\delta x^2 + \delta y^2 + \delta z^2 + \delta \psi^2 \right), \tag{13}$$

where it is considered the minimization of the heading deviations $\delta\psi$ (in rad) and of the position errors δx, δy and δz (in m) obtained by comparing pose estimations from kinematics with the ground-truth.

IV. CASE STUDY: THE J8 ROVER

The robotic rover J8 by Argo is a heavy unmanned ground vehicle that allows off-road mobility with a low center of mass, amphibious capability and a top speed of $7.5\,\mathrm{m\,s^{-1}}$ (see Fig. 3). The vehicle is 3.2 m long and 1.6 m wide. It weights 1090 kg and admits a maximum payload of 567 kg. Ground clearance of the chassis is 0.2 m. The dimensions of the base rectangle of J8 are $x_m = 0.6\,\mathrm{m}$ and $y_m = 1.06\,\mathrm{m}$.

The rover features skid-steer locomotion with eight low-pressure (5-psi) 24-inch tires and zero turning radius. It can be tele-operated through a joystick and a line-of-sight wireless link. The rover is powered by four 48 V batteries (5 kWh each) that can last up to 6 h.

The unconventional drive train of J8 does not include a motor dedicated to rotate the wheels of each tread. Instead, two electric motors are connected to the transmission, which, in turn, provides traction for both treads (see Fig. 4). The main motor drives the vehicle forward and reverse in straight-line motion. It has an electro-magnetic brake to stop motion in the event of power loss or missing control signal. The secondary motor steers the rover by adding movement to a tread and subtracting it to the other. Finally, chains are employed to convey motion to every wheel from the transmission. The rotation speed of each motor is delivered by its corresponding controller through an internal CAN bus at a rate of 20 Hz. The current tread speeds v_l and v_r can be obtained from these data.

Fig. 3. The all terrain J8 rover by Argo.

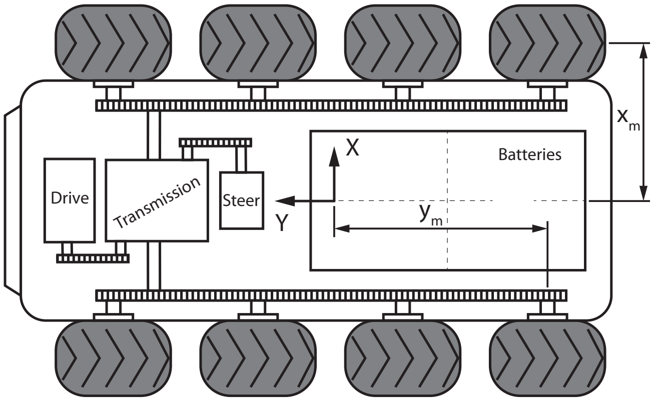

Fig. 4. Scheme of the J8 drive train from above. The local coordinate system and the dimensions of the base rectangle are shown.

A. Experimental setup

Experiments have been performed by tele-operating J8 on a smooth concrete surface with different inclines at the entrance of the Industrial Engineering School of the University of Málaga (see Fig. 5). The maximum absolute value of speeds for the traction and the steer motors of J8 have been limited to $1\,\mathrm{m\,s^{-1}}$. Thus, $v_y^m = 1\,\mathrm{m\,s^{-1}}$, although tread speeds can achieve peaks of $2\,\mathrm{m\,s^{-1}}$.

Fig. 5. Photograph of the concrete surface (Google Maps ©2024). Four sloped zones are highlighted and their mean inclination indicated.

A 3DM-GX5 Attitude and Heading Reference System (AHRS) sensor by MicroStrain, located at the origin of the J8 frame, is employed to obtain the roll and pitch angles of the vehicle every 50 ms. A RS-Helios-5515 LiDAR by Robosense, located at the front mast of J8, is used for pose estimation. This sensor provides 3D point clouds at 10 Hz with 32 simultaneous vertical channels from -55° to 15° and with a full horizontal field of view of 360°.

The open-source library `lidarslam_ros2` [42] has been employed on each experiment to produce offline the ground-truth pose every 100 ms, approximately. This ROS 2 package for 3D LiDAR SLAM employs NDT scan matching and $\mathrm{g}^2\mathrm{o}$ pose-graph optimization [43].

B. Parameter Estimation

Table I contains all the estimated parameters of ICRIK for J8. The parameters for ICRHK were obtained on the first zone of the concrete surface with $\beta = 0^\circ$ as in [23].

The correction factors in Table I are very close to 1, which means that tread speed estimations are well calibrated, being c_r slightly bigger than c_l. It can also be observed a good lateral symmetry for J8 with $\bar{x}^l_{ICR} \approx -\bar{x}^r_{ICR}$ and a small forward asymmetry with $\bar{y}_{ICR} > 0$.

Fig. 6 shows the followed path on the ground inside the 3D map built by 3D LiDAR SLAM when J8 was commanded with $V_r = -V_l = 0.33\,\mathrm{m\,s^{-1}}$ to obtain the extra parameters on the second identification stage. It can be observed that the vehicle slides down while trying to turn counterclockwise on the second zone of the concrete surface with $\beta \approx 4^\circ$.

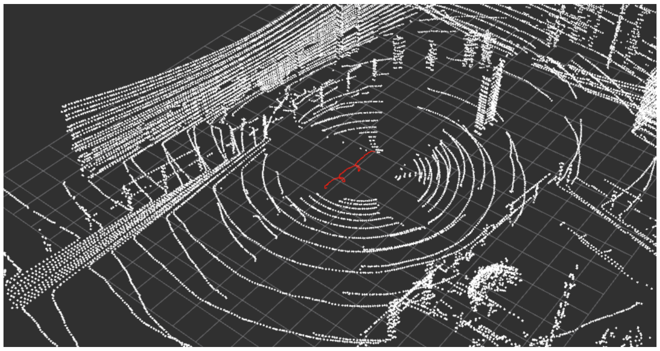

Fig. 6. Trajectory on the ground (red line) inside the 3D LiDAR map (white dots) for the second identification stage.

TABLE I
ESTIMATED PARAMETERS OF ICRIK FOR J8 ON THE SMOOTH CONCRETE SURFACE.

parameter	value	unit
c_l	1.004	
c_r	1.011	
$\bar{x}^l_{ICR}$	-0.980	m
$\bar{x}^r_{ICR}$	1.073	m
$\bar{y}_{ICR}$	0.206	m
λ_1	1.222	$\mathrm{s\,rad^{-1}}$
λ_2	4.965	$\mathrm{s\,rad^{-1}}$

C. Dead-Reckoning Validation

Three experiments have been carried out to validate the obtained ICRIK model of J8. A view from above is included to illustrate each one, where the bottom of the figures corresponds to the lowest part of the slope and the top with the highest.

The first experiment is a clockwise rotation with $V_l = -V_r = 0.3\,\mathrm{m\,s^{-1}}$ on the second zone with $\beta \approx 3.6^\circ$ (see Fig. 7a), similar to the identification path of Fig. 6. It can be observed that ICRHK is unable to predict the slide down phenomenon that ICRIK does.

In the second experiment, the rover performs an 8-shaped path on the second zone with $\beta \approx 5.3^\circ$ (see Fig. 7b). Dead-reckoning estimations with ICRIK are closer to the ground-truth path than those generated by ICRHK. The latter works better than in the first experiment since sliding down is not so pronounced.

The third experiment involves a longer trajectory (see Fig. 7c) that crosses the second, third and fourth zones of the concrete surface (see Fig. 5). It can also be observed that ICRIK is capable of enhancing ICRHK estimations. Fig. 8 contains the maximum slope β along this experiment calculated with (3) using the roll and pitch angles, where some discrepancies can be observed between the offline ground-truth and the online measurements from the AHRS sensor.

Table II contains the mean squared errors in position and heading as well as the mean fitness in the previous experiments. Errors are computed every time that `lidarslam_ros2` produces a ground-truth pose, adding N values in total. It can be observed that the mean squared errors of ICRIK are smaller than those of ICRHK in most comparisons. The mean fitness is always favorable to the ICRIK model.

TABLE II
DEAD-RECKONING ERRORS FOR ICRHK AND ICRIK ON THE THREE VALIDATION PATHS.

experiment	error	ICRHK	ICRIK
# 1 (N= 477)	$(\sum \delta x^2)/N$	0.018	0.014
	$(\sum \delta y^2)/N$	0.957	0.006
	$(\sum \delta z^2)/N$	0.007	0.001
	$(\sum \delta \psi^2)/N$	0.023	0.060
	J/N	1.005	0.081
# 2 (N= 616)	$(\sum \delta x^2)/N$	0.153	0.158
	$(\sum \delta y^2)/N$	0.503	0.054
	$(\sum \delta z^2)/N$	0.111	0.082
	$(\sum \delta \psi^2)/N$	0.014	0.016
	J/N	0.781	0.310
# 3 (N= 883)	$(\sum \delta x^2)/N$	7.808	6.028
	$(\sum \delta y^2)/N$	0.572	0.060
	$(\sum \delta z^2)/N$	0.409	0.322
	$(\sum \delta \psi^2)/N$	0.032	0.028
	J/N	8.821	6.438

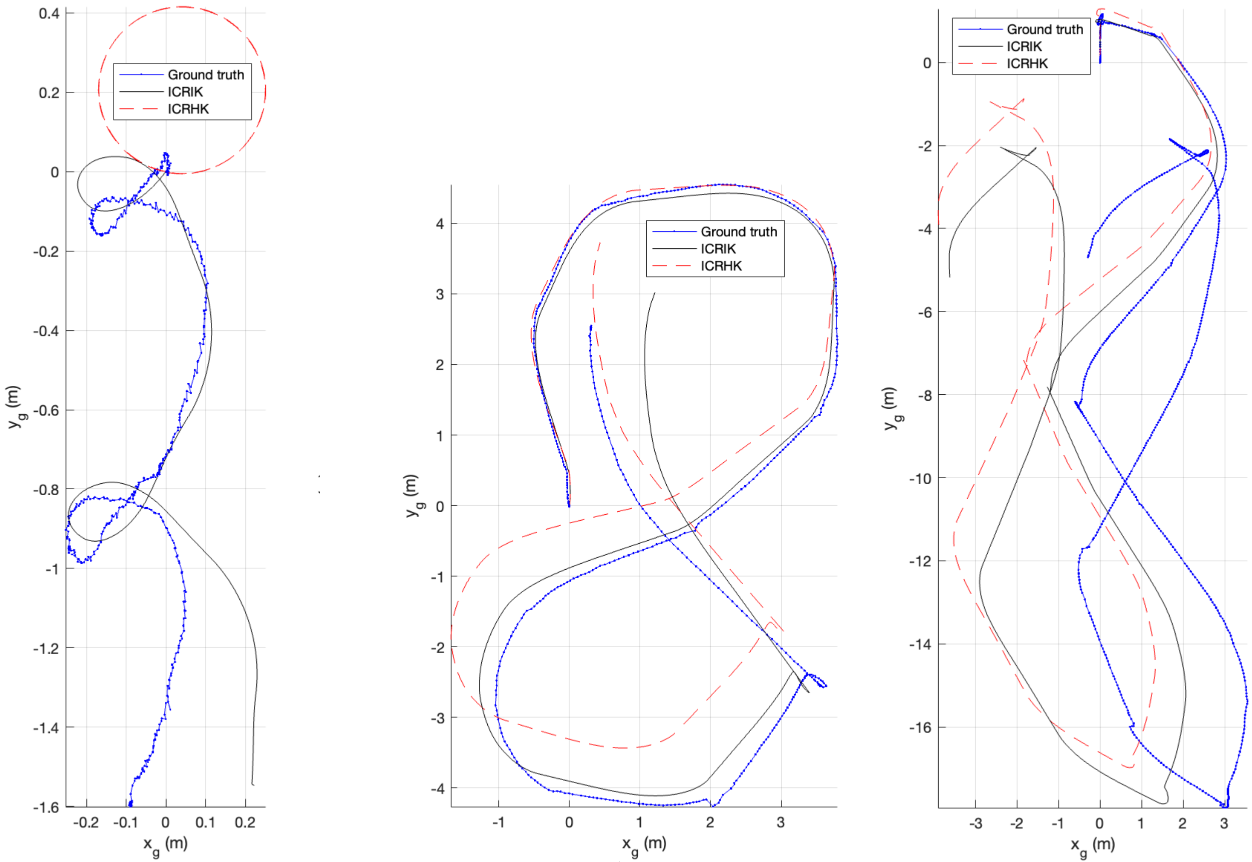

(a) (b) (c)

Fig. 7. Top view of the first (a), second (b) and third (c) validation experiments.

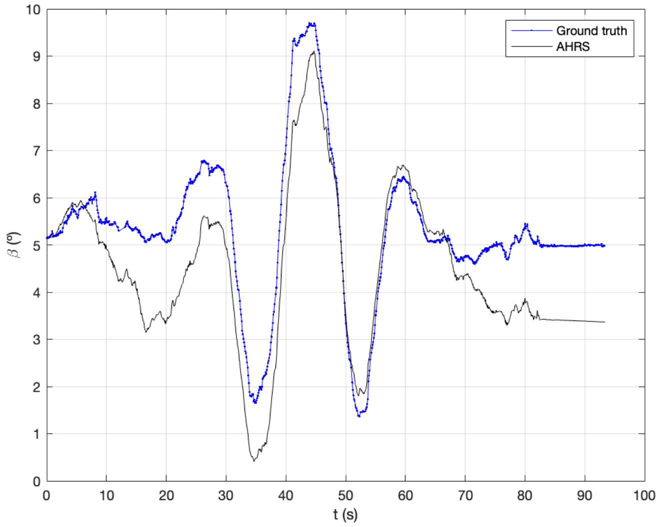

Fig. 8. Angle β along the third validation trajectory.

V. CONCLUSIONS

The main contribution of the paper is to propose a new kinematic model for wheeled skid-steer vehicles on firm slopes which is based on the instantaneous center of rotation (ICR) of the treads. The previous ICR-based horizontal model, where constant tread ICRs were considered, has been extended with two additional parameters to predict the sliding down phenomenon while turning on slopes.

The current pitch and roll angles of the vehicle together with tread speeds are employed to calculate the changing positions of tread ICRs around the horizontal values. Model parameters are estimated in two stages sequentially, being the first and the second on horizontal and inclined terrains, respectively. A simple experiment on slopes is proposed to identify the extra parameters.

This kinematic approach has been successfully applied to the 1-ton robotic rover J8 on a slanted surface of smooth concrete. Future work involves testing the ICR-based kinematics on rough inclined terrains such as asphalt. It would also be of interest to test the developed model for tracked vehicles.

REFERENCES

[1] J. Wong and W. Huang, “Wheels vs. tracks - a fundamental evaluation from the traction perspective,” *Journal of Terramechanics*, vol. 43, no. 1, pp. 27–42, 2006.

[2] S. Gorucu, B. Weichelt, and R. Burke, “Injuries and fatalities related to skid steers: 2015-2020,” *Safety*, vol. 8, no. 3, 2022.

[3] R. Khan, F. M. Malik, A. Raza, and N. Mazhar, “Comprehensive study of skid-steer wheeled mobile robots: development and challenges,” *Industrial Robot*, vol. 48, no. 1, pp. 142–156, 2021.

[4] M. A. V. J. Muthugala, K. G. S. Apuroop, S. G. A. Padmanabha, S. M. B. P. Samarakoon, M. R. Elara, and R. Y. W. Wen, “Falcon: A false ceiling inspection robot,” *Sensors*, vol. 21, no. 16, pp. 1–18, 2021.

[5] G. P. Cruz-Junior, A. M. C. Rezende, V. R. F. Miranda, R. Fernandes, H. Azpúrua, A. A. Neto, G. Pessin, and G. M. Freitas, "EKF-LOAM: An adaptive fusion of LiDAR SLAM with wheel odometry and inertial data for confined spaces with few geometric features," *IEEE Transactions on Automation Science and Engineering*, vol. 19, no. 3, pp. 1458–1471, 2022.

[6] C. Wen Zhu, E. Hill, M. Biglarbegian, S. A. Gadsden, and J. A. Cline, "Smart agriculture: Development of a skid-steer autonomous robot with advanced model predictive controllers," *Robotics and Autonomous Systems*, vol. 162, p. 104364, 2023.

[7] R. Bertoglio, V. Carini, S. Arrigoni, and M. Matteucci, "A map-free LiDAR-based system for autonomous navigation in vineyards," in *European Conference on Mobile Robots (ECMR)*, (Coimbra, Portugal), pp. 1–6, 2023.

[8] M. Toscano-Moreno, J. Bravo-Arrabal, M. Sánchez-Montero, J. Serón-Barba, R. Vázquez-Martín, J. Fernández-Lozano, A. Mandow, and A. García-Cerezo, "Integrating ROS and android for rescuers in a cloud robotics architecture: Application to a casualty evacuation exercise," in *IEEE International Symposium on Safety, Security, and Rescue Robotics (SSRR)*, (Sevilla, Spain), pp. 270–276, 2022.

[9] T. Gameiro, T. Pereira, C. Viegas, F. Di Giorgio, and N. F. Ferreira, "Robots for forest maintenance," *Forests*, vol. 15, no. 2, pp. 1–24, 2024.

[10] S. Dogru and L. Marques, "Power characterization of a skid-steered mobile field robot with an application to headland turn optimization," *Journal of Intelligent & Robotic Systems*, vol. 93, p. 601615, 2019.

[11] M. Effati and K. Skonieczny, "Systematic solution for optimally energy-efficient turning radius for wheeled skid-steer rovers," *Robotics and Autonomous Systems*, vol. 159, pp. 1–14, 2023.

[12] A. J. Prado, M. Torres-Torriti, and F. A. Cheein, "Distributed tube-based nonlinear MPC for motion control of skid-steer robots with terra-mechanical constraints," *IEEE Robotics and Automation Letters*, vol. 6, no. 4, pp. 8045–8052, 2021.

[13] A. Trivedi, S. Bazzi, M. Zolotas, and T. Padir, "Probabilistic dynamic modeling and control for skid-steered mobile robots in off-road environments," in *IEEE International Conference on Assured Autonomy (ICAA)*, (Laurel, USA), pp. 57–60, 2023.

[14] C. Ordonez, N. Gupta, B. Reese, N. Seegmiller, A. Kelly, and E. G. Collins-Jr., "Learning of skid-steered kinematic and dynamic models for motion planning," *Robotics and Autonomous Systems*, vol. 95, pp. 207–221, 2017.

[15] X. Yue, J. Chen, Y. Li, R. Zou, Z. Sun, X. Cao, and S. Zhang, "Path tracking control of skid-steered mobile robot on the slope based on fuzzy system and model predictive control," *International Journal of Control, Automation and Systems*, vol. 20, no. 4, pp. 1365–1376, 2022.

[16] G. Yamauchi, K. Nagatani, T. Hashimotoa, and K. Fujino, "Slip compensated odometry for tracked vehicle on a loose and weak slope," *Robomech Journal*, vol. 4, no. 27, pp. 1–11, 2017.

[17] M. Sutoh, Y. Iijima, Y. Sakakieda, and S. Wakabayashi, "Motion modeling and localization of skid-steering wheeled rover on loose terrain," *IEEE Robotics and Automation Letters*, vol. 3, no. 4, pp. 4031–4037, 2018.

[18] J. L. Martínez, J. Morales, A. Mandow, S. Pedraza, and A. García-Cerezo, "Inertia-based ICR kinematic model for tracked skid-steer robots," in *IEEE International Symposium on Safety, Security and Rescue Robotics (SSRR)*, (Shanghai, China), pp. 166–171, 2017.

[19] G. Huskic, S. Buck, M. Herrb, S. Lacroix, and A. Zell, "High-speed path following control of skid-steered vehicles," *International Journal of Robotics Research*, vol. 38, no. 9, p. 1124 1148, 2019.

[20] A. Joglekar, S. Sathe, N. Misurati, S. Srinivasan, M. J. Schmid, and V. Krovi, "Deep reinforcement learning based adaptation of pure-pursuit path-tracking control for skid-steered vehicles," *IFAC-PapersOnLine*, vol. 55, no. 37, pp. 400–407, 2022.

[21] I. Filip, J. Pyo, M. Lee, and H. Joe, "LiDAR SLAM with a wheel encoder in a featureless tunnel environment," *Electronics*, vol. 12, no. 4, 2023.

[22] J. L. Martínez, A. Mandow, J. Morales, S. Pedraza, and A. García-Cerezo, "Approximating kinematics for tracked mobile robots," *International Journal of Robotics Research*, vol. 24, no. 10, pp. 867–878, 2005.

[23] A. Mandow, J. L. Martínez, J. Morales, J. L. Blanco, A. García-Cerezo, and J. González, "Experimental kinematics for wheeled skid-steer mobile robots," in *IEEE International Conference on Intelligent Robots and Systems (IROS)*, (San Diego, USA), pp. 1222–1227, 2007.

[24] Y. Chen, Y. Wu, W. Zeng, and S. Du, "Kinematics model estimation of 4W skid-steering mobile robots using visual terrain classification," *Journal of Robotics*, vol. 2023, pp. 1–12, 2023.

[25] M. Li, L. Wang, W. Ren, Q. Liu, and C. Liu, "Tightly-coupled LiDAR-inertial odometry for wheel-based skid steering UGV," in *IEEE 17th Conference on Industrial Electronics and Applications (ICIEA)*, (Chengdu, China), pp. 510–516, 2022.

[26] D. Baril, V. Grondin, S. Deschenes, J. Laconte, M. Vaidis, V. Kubelka, A. Gallant, P. Giguere, and F. Pomerleau, "Evaluation of skid-steering kinematic models for subarctic environments," in *17th Conference on Computer and Robot Vision (CRV)*, (Los Alamitos, CA, USA), pp. 198–205, IEEE Computer Society, 2020.

[27] J. L. Martínez, J. Morales, M. Sánchez, M. Morán, A. J. Reina, and J. J. Fernández-Lozano, "Reactive navigation on natural environments by continuous classification of ground traversability," *Sensors*, vol. 20, no. 22, 2020.

[28] S. Feng, B. Sebastian, and P. Ben-Tzvi, "A collision avoidance method based on deep reinforcement learning," *Robotics*, vol. 10, no. 2, 2021.

[29] C. Wang, W. Lv, X. Li, and M. Mei, "Terrain adaptive estimation of instantaneous centres of rotation for tracked robots," *Complexity*, vol. 2018, pp. 1–10, 2018.

[30] L. Bao, K. Li, C. Han, K. Shin, and W. Kim, "Adaptive online steering efficiency coefficient estimation for enhanced terrain motion control in four-wheeled skid-steering mobile robots," *International Journal of Control, Automation and Systems*, vol. 21, no. 8, pp. 2444–2454, 2023.

[31] T. Wang, Y. Wu, J. Liang, C. Han, J. Chen, and Q. Zhao, "Analysis and experimental kinematics of a skid-steering wheeled robot based on a laser scanner sensor," *Sensors*, vol. 15, no. 5, pp. 9681–9702, 2015.

[32] J. Pentzer, S. Brennan, and K. Reichard, "Model-based prediction of skid-steer robot kinematics using online estimation of track instantaneous centers of rotation," *Journal of Field Robotics*, vol. 31, no. 3, pp. 455–476, 2014.

[33] X. Zuo, M. Zhang, M. Wang, Y. Chen, G. Huang, Y. Liu, and M. Li, "Visual-based kinematics and pose estimation for skid-steering robots," *IEEE Transactions on Automation Science and Engineering*, vol. 21, no. 1, pp. 91–105, 2024.

[34] G. Reina and R. Galati, "Slip-based terrain estimation with a skid-steer vehicle," *Vehicle System Dynamics*, vol. 54, no. 10, pp. 1384–1404, 2016.

[35] S. Dogru and L. Marques, "An improved kinematic model for skid-steered wheeled platforms," *Autonomous Robots*, vol. 45, no. 2, pp. 229–243, 2021.

[36] S. Rabiee and J. Biswas, "A friction-based kinematic model for skid-steer wheeled mobile robots," in *IEEE International Conference on Robotics and Automation (ICRA)*, (Montreal, Canada), pp. 8563–8569, 2019.

[37] J. Morales, J. L. Martínez, A. Mandow, A. García-Cerezo, and S. Pedraza, "Power consumption modeling of skid-steer tracked mobile robots on rigid terrain," *IEEE Transactions on Robotics*, vol. 25, no. 5, pp. 1098–1108, 2009.

[38] J. Pentzer, S. Brennan, and K. Reichard, "On-line estimation of power model parameters for skid-steer robots with applications in mission energy use prediction," *Journal of Field Robotics*, vol. 39, no. 6, pp. 763–782, 2022.

[39] M. Effati, K. Skonieczny, and D. J. Balkcom, "Energy-optimal trajectories for skid-steer rovers," *The International Journal of Robotics Research*, pp. 1–32, 2024.

[40] N. Gupta, C. Ordonez, and E. G. Collins-Jr., "Dynamically feasible, energy efficient motion planning for skid-steered vehicles," *Autonomous Robots*, vol. 41, no. 2, pp. 453–471, 2017.

[41] J. L. Martínez, J. Morales, J. M. García, and A. García-Cerezo, "Analysis of tread ICRs for wheeled skid-steer vehicles on inclined terrain," *IEEE Access*, vol. 11, pp. 547–555, 2023.

[42] R. Sasaki, "lidarslam_ros2," 2020. Accessed: 11 march 2024, https://github.com/rsasaki0109/lidarslam_ros2.

[43] Q. Serdel, C. Grand, J. Marzat, and J. Moras, "Online localisation and colored mesh reconstruction architecture for 3D visual feedback in robotic exploration missions," in *IEEE/RSJ International Conference on Intelligent Robots and Systems (IROS)*, (Kyoto, Japan), pp. 8690–8697, 2022.